Mapping of Directional Ocean Wave Spectra in Hurricanes and Other Environments

Ivan PopStefanija, *Member, IEEE*, Christopher W. Fairall, and Edward J. Walsh, *Life Senior Member, IEEE*

***Abstract*— The NOAA Wide Swath Radar Altimeter (WSRA) and its processing are described. The WSRA provides real-time measurements of sea surface significant wave height and directional wave spectra during flights in hurricanes and other environments. The characteristics of near nadir scattering from the sea surface and the resulting distortion of the wave topography measured by the WSRA are discussed, as well as the simulation which generated a matrix to correct the directional wave spectra produced from the WSRA wave topography.**

***Index Terms*— Airborne radar remote sensing, digital beamforming technique, directional ocean wave spectra, radar altimetry, sea surface electromagnetic scattering, sea surface measurements.**

I. Introduction

HURRICANES draw energy through the air/sea interface, which is characterized by the directional wave spectrum. The present ability to provide targeted measurements of sea surface directional wave spectra is the result of over 40 years of evolution. In the 1970s, the Naval Research Laboratory (NRL) developed the 36-GHz surface contour radar (SCR) under the NASA advanced applications flight experiments (AAFEs) program. The SCR produced a topographic map of the sea surface as the aircraft advanced [1]–[4]. But the volume of the antenna system and the vibration associated with the large oscillating mirror which scanned the beam could only be accommodated by a NASA research aircraft which did not fly in tropical cyclones, where knowledge of underlying ocean wave characteristics would be very valuable to the forecasters and weather modelers.

In the 1990s, the scanning radar altimeter (SRA) mode of the NASA 36-GHz multimode airborne radar altimeter [5] was developed for installation on NOAA research aircraft that were flying missions into tropical cyclones. The SRA flew for eight hurricane seasons on an NOAA WP-3-D aircraft starting in 1998 [6], [7]. The SRA documented the hurricane large scale directional wave spectrum as well as the small-scale roughness and provided useful information for modelers [8]–[13], but the complex post-processing caused a significant delay in its data availability. When the SRA was retired after the 2005 hurricane season, the need for a system that could operate unattended and provide output products in real-time was recognized.

Manuscript received July 28, 2020; revised October 8, 2020; accepted October 28, 2020. Date of publication December 22, 2020; date of current version October 26, 2021. *(Corresponding author: Ivan Popstefanija.)*

Ivan PopStefanija is with ProSensing Inc., Amherst, MA 01002-1357 USA (e-mail: popstefanija@prosensing.com).

Christopher W. Fairall and Edward J. Walsh are with the NOAA Physical Sciences Laboratory, Boulder, CO 80305-3328 USA (e-mail: chris.fairall@noaa.gov; edward.walsh@noaa.gov).

Digital Object Identifier 10.1109/TGRS.2020.3042904

II. Wide Swath Radar Altimeter (WSRA)—Instrument Description

The NOAA WSRA is a digital beamforming radar altimeter developed by ProSensing with funding from the NOAA Small Business Innovative Research (SBIR) and Joint Hurricane Testbed (JHT) programs, with additional support from the University of Massachusetts and the Defense Advanced Research Projects Agency (DARPA). The WSRA provides continuous real-time reporting of several data products: 1) significant wave height (SWH); 2) directional ocean wave spectra; 3) the wave height, wavelength, and direction of propagation of the primary and secondary wave fields; 4) rainfall rate; and 5) sea surface mean square slope (mss). During hurricane flights, the data products are transmitted in real-time from the NOAA WP-3-D aircraft through a satellite data link to a ground station and on to the National Hurricane Center (NHC) for use by the forecasters for intensity projections and incorporation in hurricane wave models.

The WSRA operates at 16 GHz and its antenna array is comprised of 62 narrow microstrip subarrays that are parallel to the aircraft heading and spaced at half-wavelength intervals orthogonal to the aircraft heading. The raw I&Q data are collected for the returns from sequential 150-MHz chirped transmissions on each of the 62 array elements. These Level0 data, acquired over a 2–3-ms interval depending on the aircraft altitude, are coherently combined to produce 80 narrow beams spread over $\pm 30^\circ$ from the overall antenna boresight. For each of the 80 narrow beams, 16 return waveforms are averaged incoherently to reduce the Rayleigh fading inherent in the backscattered power so the result well represents the range variation of the radar echo.

Level 1 data, which are the average returned power in each range gate for the selected range interval in each of the 80 narrow beams, are generated at approximately a 10-Hz rate. The range interval is chosen so that the radar backscatter from the sea surface is present in each of the 80 narrow beams. Level 1 data are high volume, and 300 consecutive sets of 80 return waveforms, acquired over 30-s intervals, are saved at 10-min intervals on the local onboard WSRA server computer for investigative and diagnostic purposes.

Level 2 data contain the centroid range to the sea surface and the integrated backscattered power for each of the

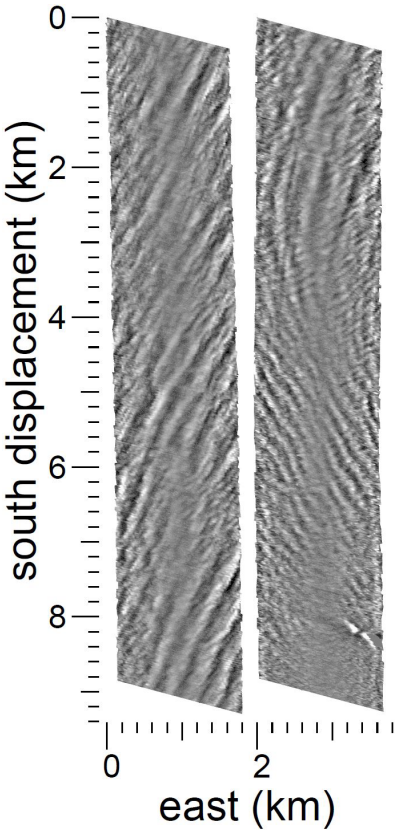

Fig. 1. Grayscale-coded wave topography from 1620 raster lines of WSRA data. The first 800 raster lines are in the left image with a grayscale spanning 5 m (white) to −5 m (black) for the top 400 lines and ±4 m grayscale for the bottom 400. The next 820 raster lines are in the right image with the top 410 lines using a ±3-m grayscale and the bottom 410 lines using ±2 m.

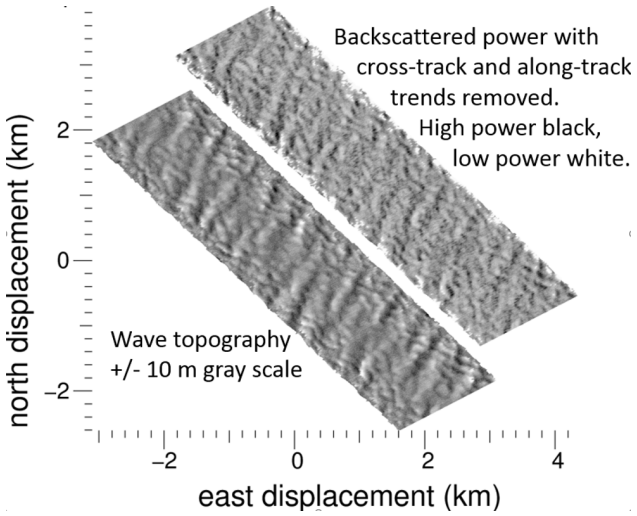

Fig. 2. WSRA wave topography image goes from −10 m (black) to 10 m (white). The sense of the backscattered power image is reversed, with the lowest power being white and the highest power being black.

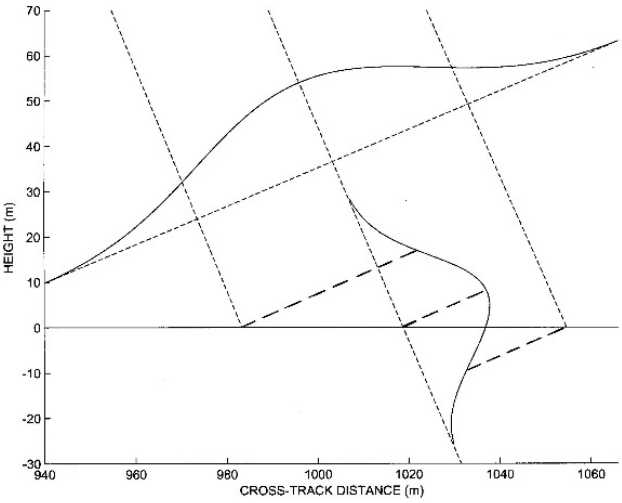

Fig. 3. WSRA narrow beam, represented by a Gaussian gain variation, boresighted on a flat sea surface from 2400 m at a 23° off-nadir incidence angle.

80 narrow beams. The aircraft flight parameters needed for accurate georeferencing of the WSRA data products are also included in the saved Level 2. At approximately a 10-Hz rate, the ranges from the 64 narrow beams nearest nadir (±23°) are multiplied by the cosines of their various incidence angles to determine the vertical distance to each position across the swath. The aircraft altitude is determined by averaging the 64 heights on each cross-track raster line and then filtering the result along-track to eliminate wave contamination. Subtracting the individual narrow beam vertical distances from the aircraft altitude produces a topographic map of the waves as the aircraft advances.

Fig. 1 shows 1620 raster lines of grayscale-coded WSRA wave topography from the 64 beams nearest nadir. The data were acquired in Hurricane Irene on August 25, 2011, while the aircraft flew south in the Bahamas at 2260-m height. The wave height variation over the 1620 raster lines was so dramatic that four different gray scales were used to make the details of the evolving wave field apparent.

The northwest tip of Whale Cay (26.714°N, 77.243°W) is apparent in Fig. 1 at 8.2-km south and 3.4-km east. The incidence plane of the narrow beams is perpendicular to the aircraft heading. A strong wind from the west required the aircraft heading to be about 15° west of south to maintain its southern flight track.

III. WSRA Measurement Geometry

Fig. 2 (left) shows a grayscale-coded map of WSRA sea surface topography in Hurricane Irene on August 25, 2011, generated from the 64 beams nearest nadir for 500 raster lines of WSRA range data acquired as the aircraft flew northwest. The right image is the backscattered power from the same beams after removing the average cross-track and along-track trends. Many details of the wave topography map are in evidence in the backscattered power image. Backscattered power varies with depth into the waves as well as with the tilts of the water surface. In turn, those variations in backscattered power distort the apparent elevation of the water surface determined by the WSRA.

The center (nadir) of the 80 narrow beams has a half-power cross-track width of 1.3° and the off-nadir beamwidths widen as $1/\cos\theta$. In the along-track direction, the antenna beamwidth is 2.1°, determined as λ/D where λ is the wavelength of the radar signal and D is the 60-cm antenna dimension in the along-track direction.

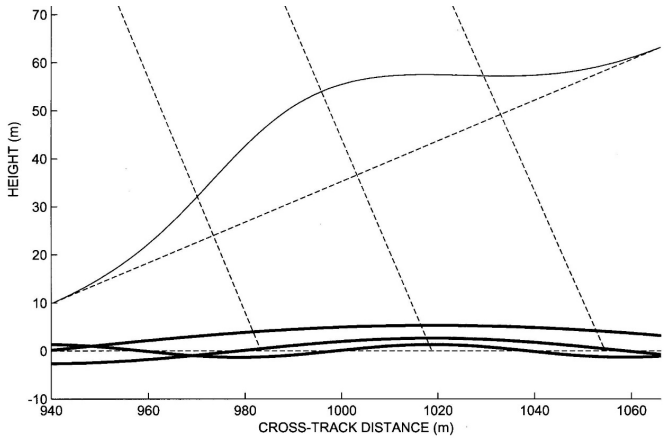

Fig. 4. WSRA narrow beam of Fig. 3 boresighted at the crest of ocean waves of 80-, 160-, and 320-m wavelength with wavelength to wave height ratios of 30.

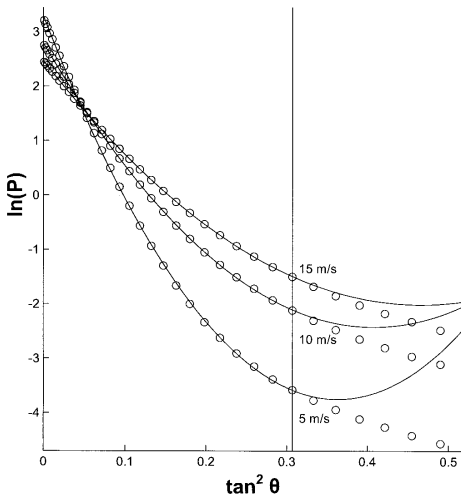

Fig. 5. 14-GHz theoretical backscattered power variation with incidence angle (circles) [18] and fitted quadratic curves (1). This is [19, Fig. 3].

Fig. 3 is drawn in proportion showing one of the WSRA 80 narrow beams, represented by a Gaussian gain variation, boresighted on a flat sea surface from 2400 m at a 23° off-nadir incidence angle. The lines of short dashes extending from the upper left indicate the beam boresight and its half-power limits. The lines of long dashes show how the gain variation across the beam would translate into the range variation of backscattered power indicated along the beam boresight. Even though the half-power range extent of the backscattered power would be more than 28 m for the angle shown, the centroid range computed by the WSRA would produce an accurate range to the surface if the sea surface radar cross section were uniform.

In Fig. 4 the geometry is the same as Fig. 3, but the three curves near the dashed mean sea level represent sinusoidal ocean waves of 80-, 160-, and 320-m wavelength with wavelength to wave height ratios of 30, which is typical for the higher waves in a hurricane. The antenna beam is boresighted at the crest of the waves.

Consider the three dashed radials (boresight and half power limits) in Fig. 4. The wave tilt on the nadir side of the crest reduces the incidence angle and increases the backscattered power. The wave tilt on the off-nadir side of the crest increases the incidence angle, reducing the backscattered power. The shortened centroid range from the skewed backscattered power distribution, assigned to the beam boresight angle, will make the wave crest appear higher than it actually is. Even though the slopes of all three sinusoidal ocean waves are identical, a shorter wavelength produces a larger slope variation within the beam and a proportionally greater apparent crest height increase.

For a wave trough at the boresight, the wave tilt on the nadir side would increase the incidence angle, reducing the backscattered power, while the tilt on the off-nadir side would reduce the incidence angle, increasing the backscattered power and skewing the centroid range longer, increasing the apparent depth of the wave trough. Wave tilt modulation increases the apparent height of waves propagating across the swath and the effect is greater for shorter wavelengths.

IV. Backscattered Power Variation With Incidence Angle

Correcting for the distortions in WSRA measured wave topography requires a model for the variation of radar cross section with incidence angle. The power backscattered from the sea surface generally decreases in an approximately Gaussian fashion within 10°–15° of nadir and then falls off more slowly at larger incidence angles [14]–[16]. The variation has been explained by an analytical sea surface slope model using the theory of the surface as a two-scale compound process, with large-scale inhomogeneities modulating a normally distributed population of smaller scales [17], and by using only Gaussian sea surface slope statistics and accounting for diffraction effects [18].

A quadratic expression [19] for the variation of backscattered power P with incidence angle

$$\ln P(S) = -AS^2 + BS^4 \tag{1}$$

where S is the sea surface slope and A and B are the linear and quadratic coefficients of the square of sea surface slope, well-matched the theoretical computation at 14 GHz [18]. The circles in Fig. 5 are the theoretical computation and the curves are the fitted quadratic equation (1), which agree well out to incidence angles of about 29°, indicated by the vertical line. A is related to the sea surface mss by

$$A = \text{mss}^{-1} - 2. \tag{2}$$

Fig. 6 shows two examples of the variation of backscattered power with off-nadir incidence angle averaged over 500-line segments of WSRA data. In the general WSRA processing, the power values from the left and right sides of the swath are averaged but they were kept separate in Fig. 6 to demonstrate their consistency.

The data in the top plot, corresponding to an mss of 0.023, were acquired in Tropical Storm Karen when the wind speed at the 2552-m altitude was 10 m/s. The data in the bottom plot, corresponding to an mss of 0.047, were acquired about 200-km north of the eye of Hurricane Irene while the wind speed at the 2449-m aircraft altitude was 37 m/s.

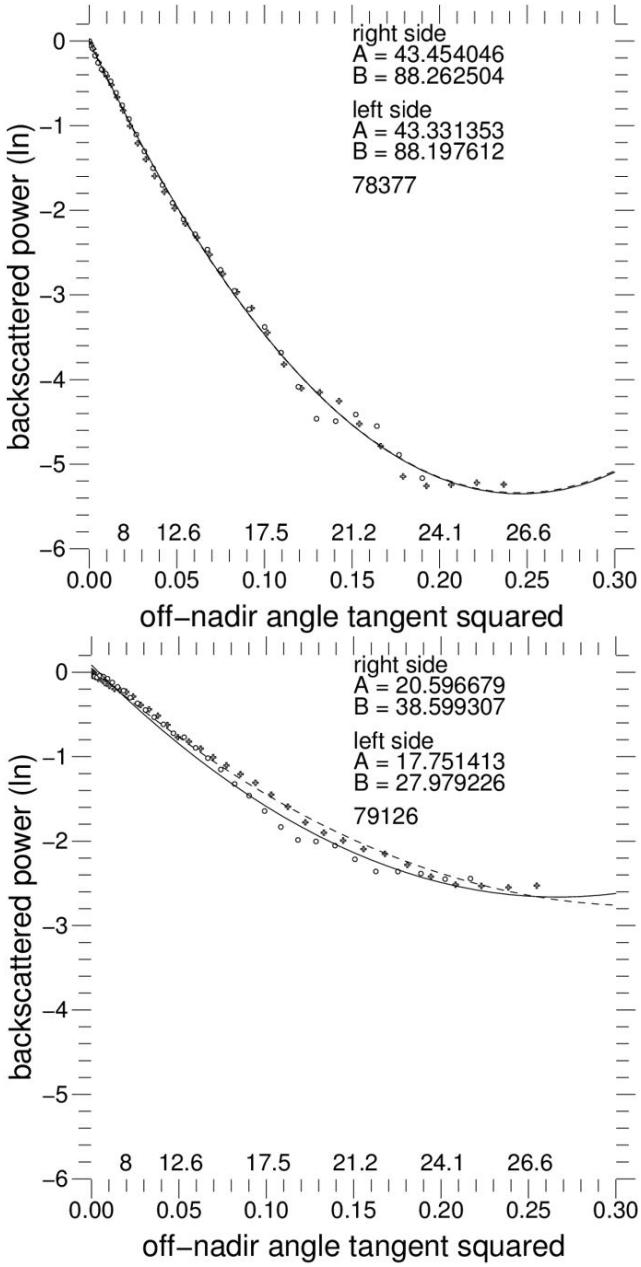

Fig. 6. Variation of backscattered power with off-nadir incidence angle averaged over 500-line segments of WSRA data. The circles show the power falloff on the right side of the swath in 0.75° increment bins and + symbols show the fall-off on the left side. The top abscissa numbers are in degrees. The curves and *A*, *B* values indicate the result of fitting (1) to the power variations on the right (solid) and left (dashed) sides of the swath. Time in seconds of day is indicated below the *A, B* values.

Fig. 7 shows all the *B* versus *A* values determined from WSRA data for four flights. The aircraft altitude was always between 2 and 2.6 km except that about half the low wind test flight data were acquired at 1.6 km. The curve in Fig. 7 is the power law

$$B = 0.4182\ A^{1.434} \tag{3}$$

that best fits all the 36-GHz NASA SRA data acquired in the Southern Ocean [19] for wind ranging from 2 to 19 m/s and waves ranging from 1- to 9-m wave height. The general

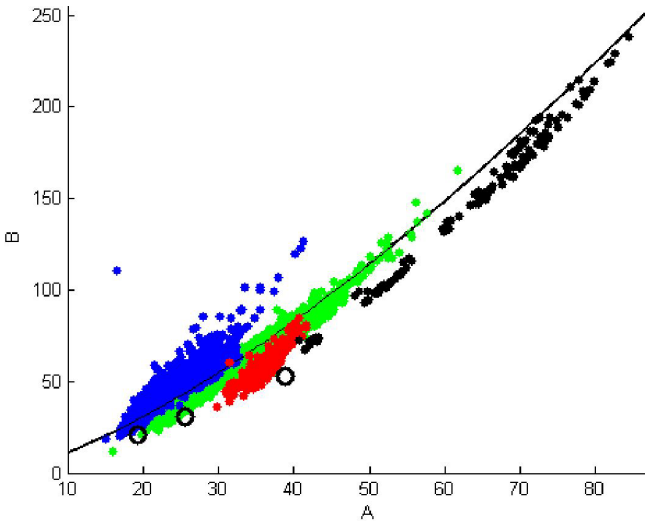

Fig. 7. *B* versus *A* values determined from WSRA 16-GHz data for four flights: 1) hurricane Irene in the Atlantic Ocean on August 25, 2011 (blue); 2) tropical Storm Karen in the Gulf of Mexico on October 3, 2013 (green); 3) Calwater 2015 in the Pacific Ocean on February 9, 2015 (red); and 4) a low wind test flight in the Gulf of Mexico in 2015 (black). The three open circles are from the [18] theoretical computation at 14 GHz.

variation of the WSRA 16-GHz data follows the power law that best fits the 36-GHz SRA data.

For every 10-s nonoverlapping set of 100 raster lines of WSRA wave topography, the real-time automated processing during the flights determines coefficient *A* from the average of the power falloff on the left and right sides of the swath within 14° of nadir and converts that to an mss value using (2).

V. Numerical Simulation of Wave Topography Distortions

A 3-D numerical simulation was developed which projected the measured gain variation for the WSRA narrow beams, broken into 0.025° elements in the along-track plane and 0.05° elements in the cross-track plane, onto a long-crested sinusoidal ocean wave. The range to the sea surface for each beam subelement, weighted by its gain and the radar cross section determined from the specified mss, (1)–(3) and the local incidence angle, produced the range variation of backscattered power whose centroid, ascribed to the beam boresight, determined the apparent surface elevation.

Fig. 8 shows the wave profiles on the right side of the WSRA swath which were generated by the simulation for an aircraft altitude of 2.5 km and long-crested sinusoidal waves propagating across the swath. The greatest variations in apparent wave height occurred for the lowest mss value, 0.02. For the 320-m wavelength, the apparent wave height increased by about a factor of 2.5 toward the swath edge. For the 160-m wavelength, the nadir wave height was noticeably reduced and then the wave height increased by about a factor of 5.5 by the edge of the swath, almost reaching the apparent height of the 320-m wavelength. The 80-m wavelength apparent wave height was greatly reduced at nadir, significantly increased toward the swath edge, and significantly distorted in profile.

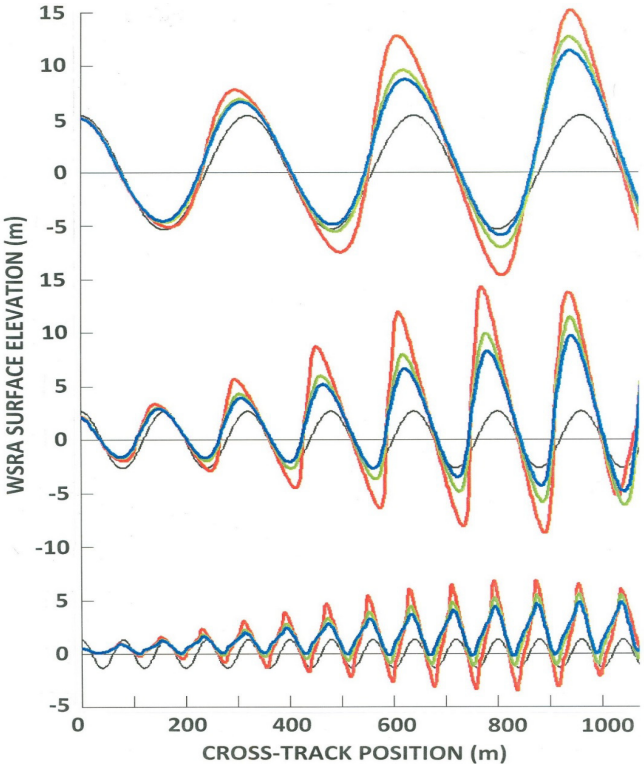

Fig. 8. Simulated WSRA-observed wave profiles generated for an aircraft altitude of 2.5 km and long-crested sinusoidal waves propagating across the swath with wavelengths of (Top) 320 m, (Middle) 160 m and (Bottom) 80 m and mss values of 0.08 (blue), 0.05 (green) and 0.02 (red). Black curves indicate the actual wave profiles with wavelength to wave height ratio of 30.

If the wave propagation direction had been parallel to the aircraft flight direction, there would have been no tilt modulation of the incidence angle by the long crests of the waves extending in the plane of incidence of the WSRA beams.

A correction matrix was generated for 17 different wavelengths (37–800 m) propagating in seven different directions (0°–90°) relative to the plane of incidence of the narrow beams for seven different values of mss (0.08, 0.065, 0.05, 0.035, 0.027, 0.02, 0.0125).

Twenty-seven narrow-beam boresights were used (0°–26° off-nadir) to determine how the apparent wave height would vary across the WSRA swath. For each beam boresight, the computation was repeated 36 times with the phase of the ocean wave at the boresight incrementing from 0° to 350° to establish a measured wave profile and determine the apparent wave height for the off-nadir angle of the beam boresight.

In general, the apparent wave height near nadir will be less than the actual wave height and the apparent wave height near the swath edges will be greater. The simulation computes the overall average of the variance for the apparent wave height variation over the entire swath.

There is less power returned to the radar as the off-nadir incidence angle increases because of reduced antenna gain and the falloff of radar cross section. If it rains, the attenuation initially reduces the WSRA signal below a useable level at the edges of the swath and then progressively narrows the swath as the rain rate increases. The effective incidence angle

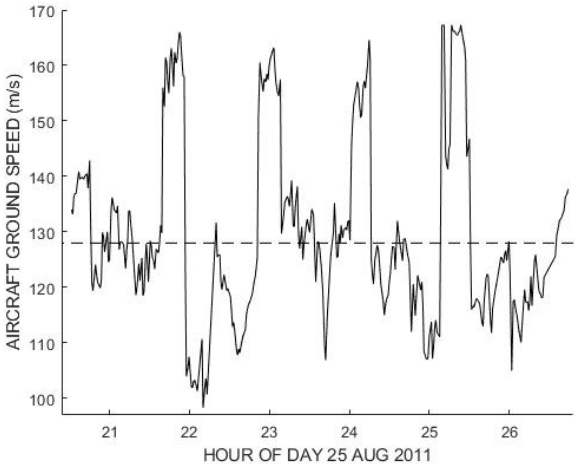

Fig. 9. Ground speed variation during the flight into Hurricane Irene on August 25, 2011.

width of the swath is taken into account in determining the wave spectral variance correction.

When correcting spectral data acquired at heights other than 2500 m, the wavelength entry into the correction matrix is simply scaled. A 160-m wavelength observed from 1.25-km height would look like a 320-m wavelength observed from 2.5-km height.

VI. Directional Wave Spectra

During the flights the WSRA data are collected continuously without gaps, and the measured sea surface elevations are stored in Level 2 (L2) files containing 2700 raster lines, where each line contains a cross-track swath of 80 elevations. A segment of wave topography (segment size: 300 lines along the track by 64 near-nadir elevations cross-track) is interpolated onto a square grid of 256 × 256 points spaced at 10-m intervals, centered on the 300 lines and oriented in the aircraft flight direction.

At an aircraft ground speed of about 85 m/s, 300 cross-track raster lines of elevations in the along-track direction are contained within the 256 × 256-point square grid. At higher aircraft ground speeds, the separation between raster lines increases in the along-track direction and fewer lines are contained within the square grid. Fig. 9 illustrates the large variation of the aircraft ground speed during the flight in Hurricane Irene on August 25, 2011. The aircraft made five passes through the eye. On the four intervening legs, where it was repositioning for the next eye pass, the strong tailwind increased the ground speed to about 170 m/s.

Fig. 9 indicates a ground speed of 128 m/s (horizontal dashed line) is a reasonable approximation for the aircraft ground speed during the eye passes. At that speed, only the center 200 of the 300 WSRA raster lines would be contained within the 256 × 256-point square grid used to produce the individual spectra.

A 2-D FFT transforms the gridded elevations into an individual directional wave spectrum. Twenty-five interpolated square grids of elevations are produced from each 2700-line L2 file while incrementing the starting line number by 100 for each individual spectrum. The WSRA Level 3 (L3) spectra

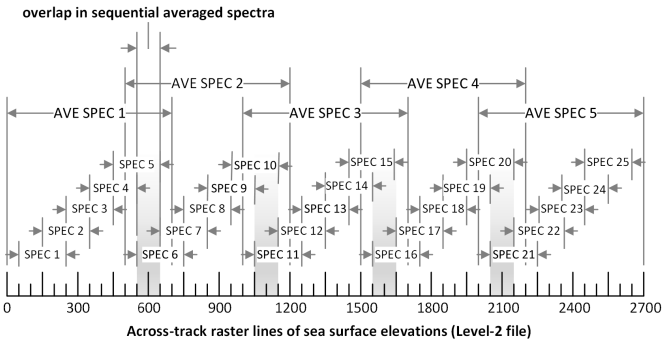

Fig. 10. WSRA data processing timing diagram for calculating L3 output spectra for a ground speed of 128 m/s. The individual spectra contain 200 raster lines at a ground speed of 128 m/s, and 150 and 300 raster lines at ground speeds of 170 and 85 m/s.

are averages of five consecutive individual spectra so the 2700 raster lines of elevations in each L2 file produce five L3 average spectra. Fig. 10 shows the data processing timing diagram for calculating L3 output spectra from raster lines of sea surface elevations stored in the L2 file. The overlap in consecutive L3 output spectra is 10% for ground speed of 128 m/s, while at low (85 m/s) and high (160 m/s) values for ground speed the overlap would be about 20% and 7%, respectively.

Level 3 spectra, along with other environmental characteristics derived from the WSRA data such as sea surface mss and rain rate, as well as the aircraft flight parameters, are transmitted in data packets every 4.5 min via a satellite data link to a ground station. The WSRA operates unattended during the flights and the data acquisition and processing is independent of the environment, whether it is a hurricane in the Atlantic Ocean or a uniform wave field in the Pacific Ocean. For a hurricane, the only human input in the ground station processing is to ensure that the latest hurricane position is included.

Level 4 (L4) spectra, generated by the ground station processing, are the final data product, resulting from deleting the artifact lobes (described in Appendix A) and Doppler-correcting and variance-correcting the L3 spectra.

The L4 output spectra have 65 × 65 spectral values-oriented in a north and east reference frame and centered on zero wavenumber. The spacing of the points in the k-space is 0.002454 rad/m. The east wavenumber values of the columns vary from −0.07854 (left) to 0.07854 (right). The north wavenumber values of the rows vary from −0.07854 (line 1) to 0.07854 (line 65). The shortest wavelength along the coordinate axes is 80 m (0.07854-rad/m wavenumber) and 57 m (0.01111-rad/m wavenumber) at the spectrum corners. The spectrum variance numbers are in m^2. To obtain spectral densities in m^4/rad^2, divide the variance values by $6.024 * 10^{-6}$ rad^2/m^2, the area covered by each spectral point. The wavenumber vectors, representing x and y coordinates for each point in the WSRA directional spectra are stored in L4 files as variables: "wavenumber_east" for x-axis and "wavenumber_north" for y-axis.

The WSRA processing calculates SWH from the L4 directional wave spectra, now fully corrected, as four times the square root of the spectra's zeroth-order moment. The WSRA calculates SWH at 50-s intervals. At an altitude of 2500 m and a ground speed of 128 m/s, the WSRA SWH estimate represents approximately 14-km^2 area of the ocean.

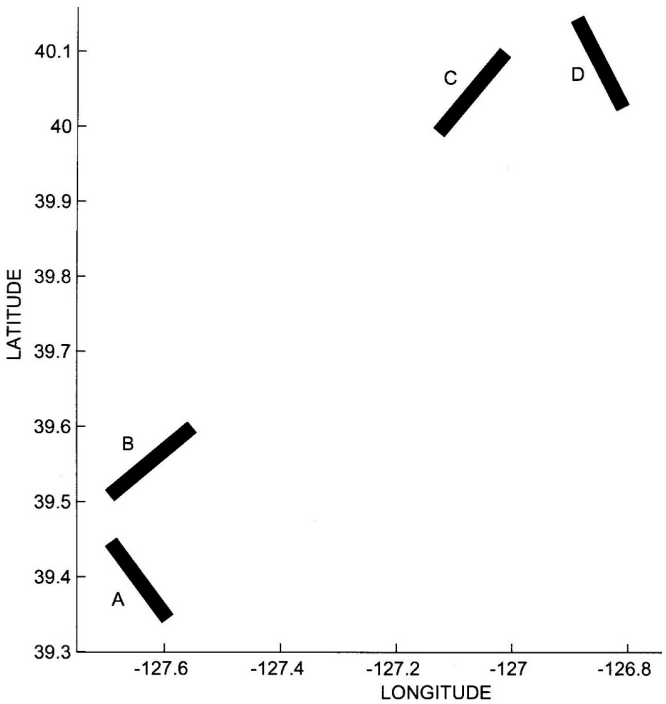

Fig. 11. Four areas of interest during the CalWater 2015 experiment flight on February 9, 2015. Each area contained 1300 raster lines of WSRA topography.

VII. Validation Analysis of WSRA Directional Wave Spectra

A flight on February 9, 2015, during the CalWater 2015 experiment [20] provided an excellent opportunity to exhibit the scattering distortions of the wave topography measured by the WSRA and the ability of the automated processing algorithm to correct the output directional wave spectra. Fig. 11 shows four areas that were about 300 km off the California coast. Each area contained 1300 raster lines of WSRA data which will be analyzed in detail.

The environmental conditions were such that the wave field could be assumed to vary slowly spatially. Fig. 12 shows 1700 raster lines of WSRA wave topography collected while the aircraft was flying northwest and the wind at the 2380-m aircraft height was blowing toward the east at 9.8 ± 0.4 m/s. Segment A in Fig. 11 included 1300 of those 1700 raster lines.

It was an unusual situation in that there were two wave systems of comparable wavelength and wave height propagating at right angles to each other. Fig. 13 shows three L4 spectra generated from the wave topography of Fig. 12.

Fig. 13 spectra provide a sense of the variability existing in the spectra of a nominally uniform wave field. The secondary wave field, a southeast propagating swell, was probably an old system and its characteristics showed little variation in wave height (3.4, 3.4, 3.3 m) and propagation direction (143°, 143°, 140°) with a peak wavelength of 201 ± 12 m. Still, its peak spectral variance varied by a factor of almost 2.

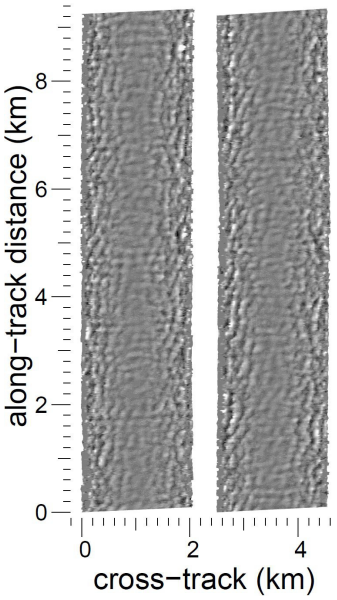

Fig. 12. Wave topography generated from 1700 consecutive raster lines of WSRA data acquired while the aircraft was flying northwest, displayed with a ±9-m grayscale. (Right) First 850 raster lines (bottom to top). (Left) Next 850 lines.

The northeast propagating wave system was broader and showed more variability with the propagation direction varying by 27° and the peak wavelength varying by 68 m.

In the first two sets of 1300 raster lines of WSRA wave topography shown in Fig. 11, the aircraft flight direction was initially aligned with one of the systems when it was flying northwest (A) and then it turned toward the northeast (B) and was aligned with the other system.

To demonstrate the effectiveness of the variance correction simulation, directional wave spectra were generated from each set of 1300 raster lines of WSRA topography from the areas identified in Fig. 11. The four spectra shown in Fig. 14 were each an average of 11 individual spectra instead of the standard 5-spectra averages of Fig. 13. This was a compromise between reducing the inherent variability in the wave spectra and keeping the result localized.

The three spectra in Fig. 13 were generated from raster lines 1001–1700, 1501–2200, and 2001–2700 in the L2 file starting at 21:30:48 UTC. Spectrum A in Fig. 14 was generated from raster lines 1301–2600 of that same L2 file. Shortly after the next L2 file began at 21:34:57 UTC, the aircraft turned toward the northeast. Spectrum B was generated from lines 601–1900 when the aircraft was flying straight and level again.

Spectrum C was generated from raster lines 1301–2600 of the L2 file that began at 21:43:14 UTC. When the next L2 file began at 21:47:22 the aircraft was still flying northeast. After it turned toward the southeast, raster lines 1101–2400 were used to generate spectrum D.

In the automated processing, an area surrounding the spectral peak is zeroed out and the peak of what remains determined. If a saddle point exists between the spectral peak and the secondary peak, the azimuth of the minimum value determines the partition boundary between the primary and secondary wave fields. For the spectra of Fig. 14, the partition boundary was fixed at 105° for consistency because the automated processing placed the partition boundary for spectrum D at 74°.

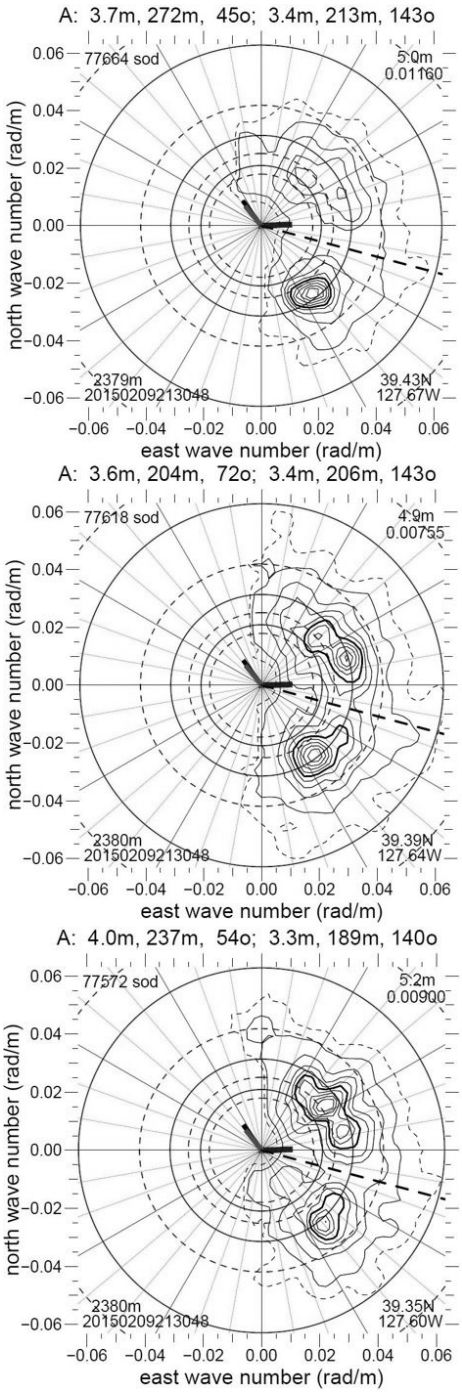

Fig. 13. L4 directional wave spectra generated from Fig. 12 wave topography. The upper right corner of each Fig. 13 spectrum contains the total $H_{1/3}$ and the spectrum peak variance in m^2. There are nine solid contours uniformly spaced from 0.1 to 0.9 of the spectral peak with a wide 0.5 contour and a dashed contour at the 0.05 level. The spectrum headers contain wave height, wavelength, and direction of propagation of the primary and secondary wave fields. A dashed radial separates the primary and secondary wave fields. The top left corner contains the seconds of the day for the center of the data span used to generate the spectrum. The bottom left corner contains the aircraft height and year, month, day, hour, minute, second of the start of corresponding L2 file. Latitude and longitude are in the bottom right corner. The short radial pointing east is wind speed (m/s)*0.001 in the downwind direction at the aircraft altitude. The short radial pointing about 325° is the aircraft track.

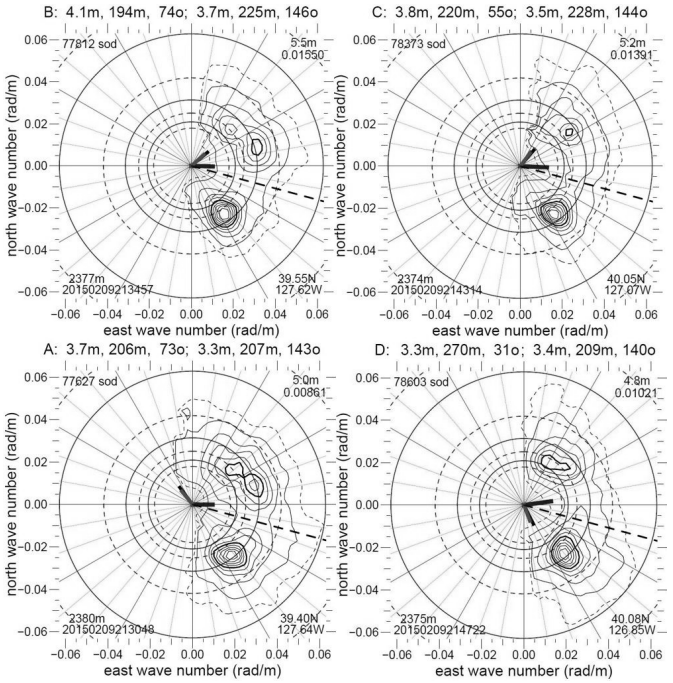

Fig. 14. Wave spectra generated from sets of 1300 raster lines of WSRA wave topography contained in the areas indicated in Fig. 11. The spectrum annotations are the same as Fig. 13. The short radials pointing east indicate wind speed (m/s)*0.001 in the downwind direction at the aircraft altitude. The short radials indicating the aircraft track are pointing NW at position A, NE at positions B and C, and SE at position D.

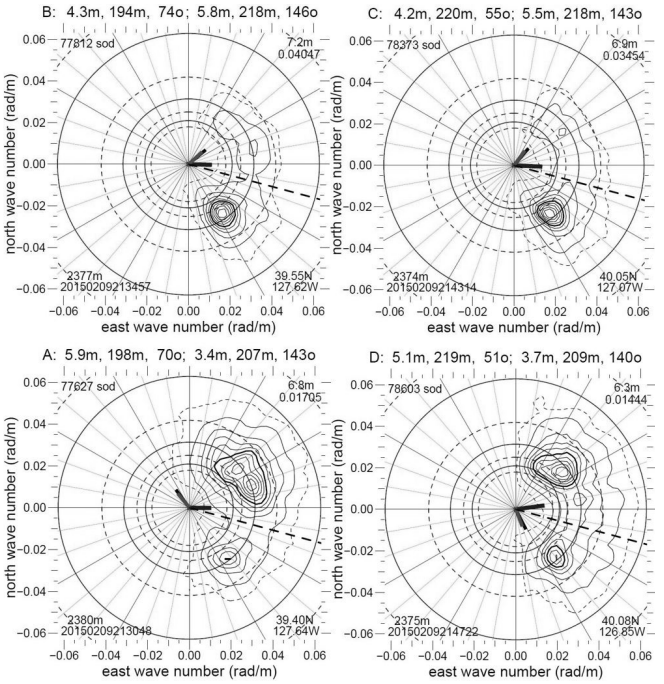

Fig. 15. Same wave spectra of Fig. 14, but before variance correction.

For the southeast swell, the average of the header information at position AB was 3.5-m wave height propagating toward 144.5°. At position CD it was 3.45-m wave height propagating toward 142°, nearly identical.

For the northeast wave system, the header information averaged 3.9-m wave height propagating toward 73.5° at AB and 3.55-m wave height propagating toward 43° at CD. The northeast wave system evolved more spatially than the southeast system and that is apparent in the wave spectral contours. The northeast wave system was bimodal in the AB area with a 200-m wavelength component propagating toward 73° and a 250-m wavelength component propagating toward 50°. At position CD the northeast wave field was more narrow, oscillating about 250-m wavelength and 45° propagation direction.

The variance-corrected wave spectra of Fig. 14 document a complex but slowly evolving wave field. Fig. 15 shows the same four spectra before the variance correction. At position AB the header information is nearly identical before and after the variance correction for the wave system which happened to be aligned with the aircraft flight direction, the southeast swell at position A, 3.4 m, 207 m, 143° (before, Fig. 15) versus 3.3 m, 207 m, 143° (after, Fig. 14), and the northeast wave system at position B, 4.3 m, 194 m, 74° (before, Fig. 15) versus 4.1 m, 194 m, 74° (after, Fig. 14).

The big distortion in wave topography results from backscattered power modulation by the surface tilts of waves propagating perpendicular to the aircraft heading. At position A the northeast wave system height was 59% higher before the variance correction (5.9 versus 3.7 m). At position B the southeast swell was 57% higher before the correction (5.8 versus 3.7 m). The peak wavelengths were also shorter before the correction (198 versus 206 m at A and 218 versus 225 m at B) because the wave topography distortion is greater for shorter wavelengths.

The Fig. 15 spectral contours dramatically document the wave tilt modulation distortion effect without considering any of the numbers. Without the variance correction, the northeast wave system was dominant at location A. But just after turning the corner, the southeast swell was dominant at location B. The southeast swell maintained its dominance while the aircraft traveled 70 km up to location C, but when the aircraft turned toward the southeast it immediately lost its dominance at location D.

The filled circles in Fig. 16 show the cross-track variation of the apparent wave height, computed as four times the standard deviation of the elevations at each of the 64 cross-track positions of the wave topography. They were generated from segments of 300 consecutive raster lines approximately centered on the raster line segments used to generate the spectra of Figs. 14 and 15. The open circles indicate the number of valid elevations at each cross-track position.

Since there is only spatial filtering by the antenna footprint at nadir, the minimum wave height values at all four locations (A–D) are about 3.3 m. The wave tilt backscattered power modulation distorting the wave topography increases as the mss decreases. The dramatic wave height increases to about 20 m at the swath edges for locations A–C result from the low mss, 0.027. The wave height increase may have been less at position D because Fig. 14 indicates the perpendicular to the aircraft heading was more than 30° off the spectral peak propagation direction.

The number of valid elevations tends to decrease very rapidly after it has declined to 80%. The automated processing

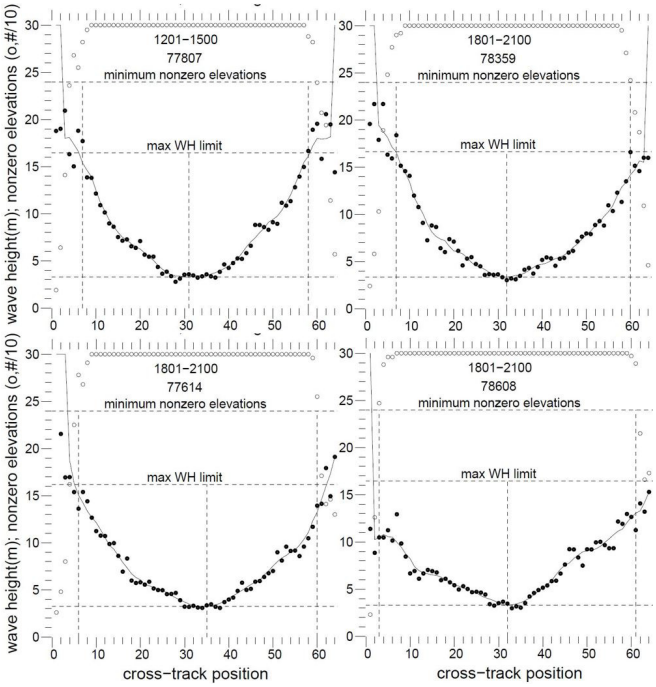

Fig. 16. Cross-track variation of the apparent wave height (filled circles) at locations A–D in Fig. 11, computed as four times the standard deviation of the elevations at each of the 64 cross-track positions of the wave topography, computed from segments of 300 consecutive raster lines. Open circles indicate the number of valid elevations at each cross-track position. The relative positions of the four data sets within this figure are the same as in Figs. 14 and 15. The five-digit numbers are seconds of the day.

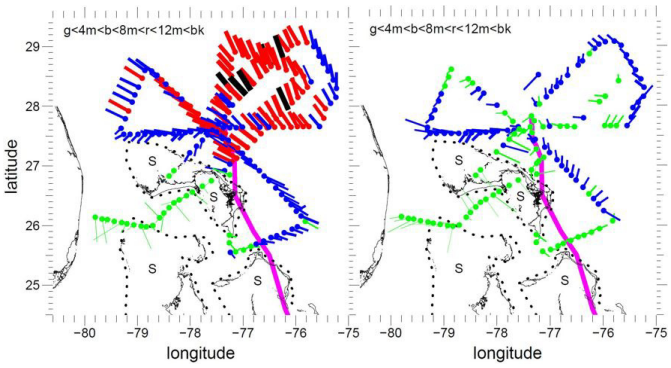

Fig. 17. Geographic coordinate vector maps of the WSRA (Left) primary and (Right) secondary wave fields during the Hurricane Irene flight on August 25, 2011. The colored dots indicate some of the locations of WSRA directional wave spectra. Radials extend from the observation locations in the wave propagation direction a distance proportional to the wavelength of (left) primary and (right) secondary wave fields. The width of the radials is proportional to wave height and they are color-coded in four-wave height intervals: green $<$ 4 m $<$ blue $<$ 8 m $<$ red $<$ 12 m $<$ black. The magenta curve shows the track of Irene. Four areas of shallow water ($<$10 m depth) in the vicinity of the islands are indicated by *S* enclosed by dots.

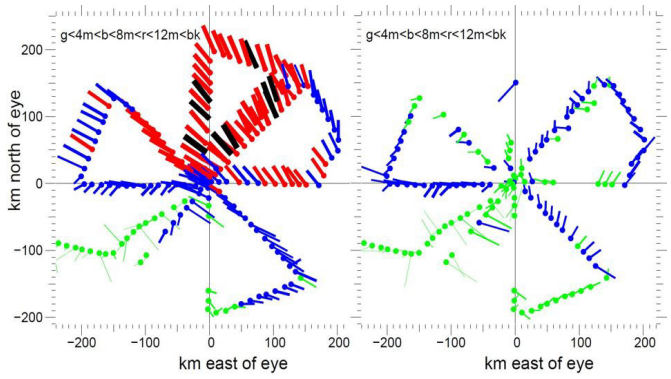

Fig. 18. Hurricane Irene storm-relative wave vector maps using the same format as Fig. 17.

generating each of the 25 individual spectra from the L2 files zeros out all elevations at cross-track positions which have fewer than 240 valid elevations in the 300-line segment, indicated by the top horizontal dashed lines in Fig. 16.

The automated processing also zeros out elevations at cross-track positions where the wave height exceeds five times the nadir wave height. That limit is indicated by the middle dashed horizontal line. To keep random fluctuations from complicating the procedure, the cross-track variation of the wave height values is filtered by a five-point moving average, indicated by the line through the filled circles.

The middle dashed vertical line and the lower dashed horizontal line indicate the cross-track position of the wave height minimum and its value. The left and right vertical dashed lines indicate the more restrictive of the two editing criteria. The 80% valid elevations are generally the more restrictive criterion and that is the situation at locations A and D. But because of the low mss and the orientation of the wave systems, the other criterion was more restrictive at location B and at the left side of the swath at location C.

FFTs represent topography as a linear superposition of long-crested sinusoids. The simulation generating the wave spectrum variance correction matrix computed the distorting effect of power backscattered from the surface areas of individual long-crested sinusoidal waves that do not exist in the real world. In the real world, the orientation of the sea surface area backscattering the power is a composite result of all the waves present. It is not obvious that the backscatter from the actual sea surface would be the same as a superposition of the backscatter from the individual long-crested sinusoidal waves of the simulation. In a hurricane the wave field generally varies rapidly spatially, making it difficult to assess the performance of the correction. However, the complex but slowly varying wave field observed during Calwater 2015 (Figs. 11–16) demonstrated that the spectral variance correction matrix is effective in correcting even the large topographic distortions resulting from a low mss environment.

VIII. Hurricane Irene Wave Field Map

Figs. 17 and 18 show some of the wave field information that the WSRA provides in real-time. In geographic coordinates, Fig. 17 shows vector maps of the WSRA primary and secondary wave fields observed during the August 25, 2011 flight into Hurricane Irene.

To reduce the amount of overlap of the radials, subsequent locations plotted had to be at least 10 km from the previous location. At the typical 128-m/s ground speed of the aircraft, there is about 6 km between adjacent L4 output directional wave spectra, so only about every other L4 spectral

location is displayed in Figs. 17 and 18. Data from locations where the wave topography was contaminated by land were excluded.

The complex geographic environment of the Hurricane Irene flight significantly affected the wave height spatial variation. The automated artifact lobe deletion process discussed in Appendix A does not consider the presence of land or shallow water, but it still produced excellent results in general.

Irene was tracking a little west of north at about 5 m/s and moved about 85 km during the 4.7 h between the first and fifth eye penetrations on the August 25 flight. Fig. 18 presents the WSRA data in a storm-relative reference frame.

The primary and secondary wave fields are automatically assigned on a basis of wave height. In regions where the wave height of two wave systems is approximately the same, the assignment can appear to switch back and forth randomly, such as in the vicinity of 0 km N, -120 km E in Fig. 18.

North of the eye the wave field was less affected by the islands and shallow water and showed the typical hurricane complexity. The wind and primary wave directions were nearly aligned in the right front quadrant of Fig. 18 (100 km N, 100 km E). In the left front quadrant (100 km N, -160 km E) there was a secondary wave field nearly aligned with the local wind, but the primary waves propagated almost orthogonal to the wind. The relative variation of the wind and wave directions could impact things like flow separation and energy transfer at the surface.

IX. WSRA Output Data Products

The Level-4 data products produced by the WSRA real-time processing include: 1) SWH; 2) directional ocean wave spectra; 3) the wave height, wavelength, and direction of propagation of the primary and secondary wave fields; 4) rainfall rate; and 5) sea surface mss. The sampling interval of the wave spectra and SWH is 50 s, resulting in a spatial resolution of approximately 5.5–8 km in along-track direction and 2 km in across track direction.

The WSRA Level-4 data products are also archived for further postflight analysis. The WSRA L4 files are formatted in Network Common Data Format (netCDF), ensuring compatibility with a large number of visualization and data analysis software applications.

Definitions of all variables present in the WSRA Level-4 data file (in the netCDF format) are shown in Appendix B. Variable names used in the netCDF file are highlighted in bold. The output wave spectra are contained in directional_wave_spectrum. Because the automated artifact lobe deletion process might occasionally delete the wrong lobe, a Level-3 wave spectrum file is also included (directional_wave_spectrum_180) in which all spectral components (real and artifact) have been Doppler and variance corrected (Figs. 19 and 20). This allows an investigator to evaluate WSRA directional ocean wave spectra without being subject to the artifact lobe deletion algorithm.

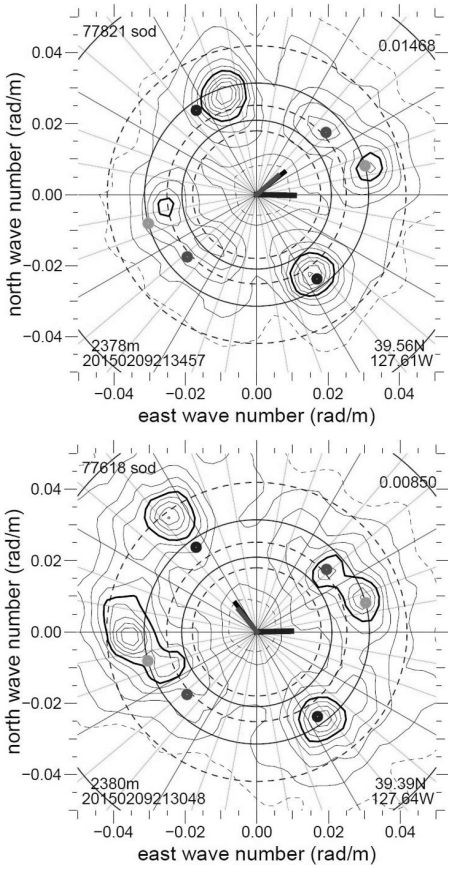

Fig. 19. WSRA directional wave spectra from the Calwater 2015 flight on February 9, 2015, that have been Doppler- and variance-corrected without deleting the artifact lobes. The gray and black dots are perfectly symmetrical reference points in identical positions in the two spectra. The radials pointing east indicate the downwind direction at the aircraft altitude. Radials pointing (Top) northeast and (Bottom) northwest indicate the aircraft flight track.

The WSRA Level-4 files containing output data described in Appendix B are available to the public for download without limitation at https://www.prosensing.com/wsra-level-4-data/.

X. Conclusion

The WSRA can provide real-time targeted measurements of wave fields in hurricanes and other environments. The 180° ambiguity present when wave topography maps are transformed into directional wave spectra can generally be eliminated automatically in the vicinity of a hurricane by using a model to simulate the integrated forcing effect of the wind field. Variations in the backscattered power caused by the tilts of the sea surface waves being measured can distort the apparent wave topography, but the spectral variance correction matrix developed is effective in correcting for even the large topographic distortions occurring in a low mss environment.

The NASA SRA, the forerunner of the NOAA WSRA, measured the storm surge in Hurricane Bonnie [21]. The WSRA could also provide targeted measurements of storm surge if the absolute height of the aircraft was determined by GPS so the WSRA wave topography maps could be vertically positioned in reference to the geoid.

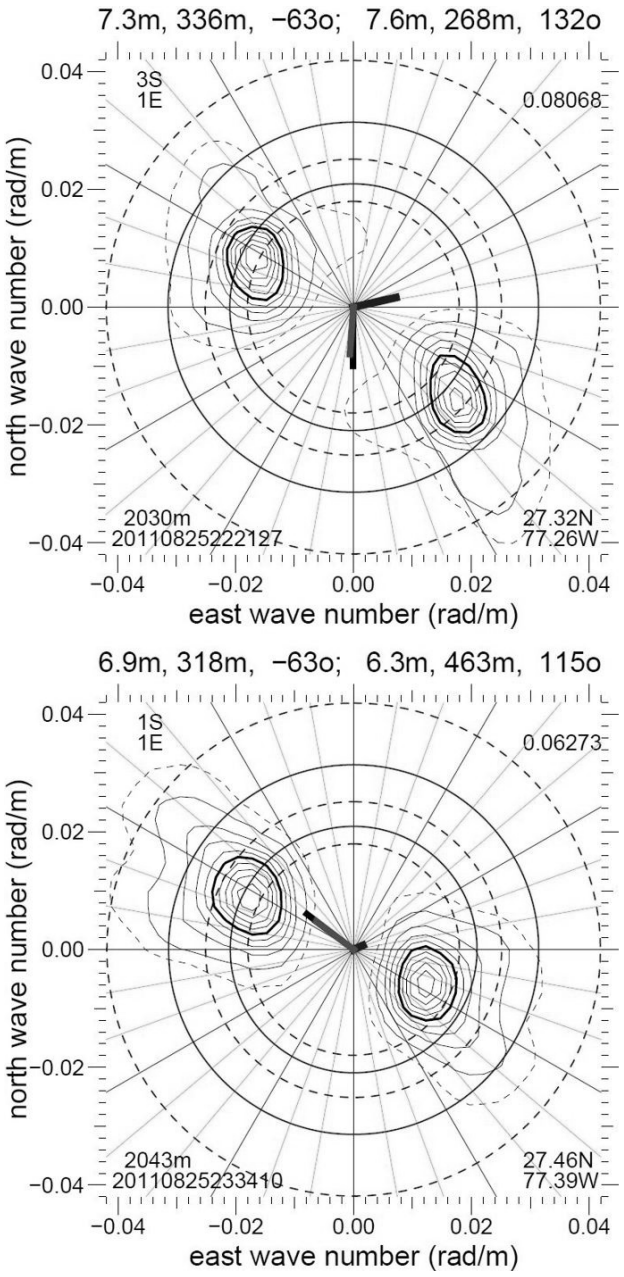

Fig. 20. WSRA directional wave spectra from Hurricane Irene that have been Doppler- and variance-corrected without deleting the artifact lobes. Top left corner numbers are km displacements from the eye.

APPENDIX A
ARTIFACT SPECTRAL LOBE DELETION

Two wave systems are apparent in the Fig. 2 wave topography image. A long wave system was nearly aligned with the aircraft flight track and a shorter wave system propagated orthogonal to the track. It is not possible to tell from the topography if the long waves were traveling northwest or southeast or if the short waves were traveling southwest or northeast. The 2-D FFT which generates Level 3 ocean wave spectra deposits half the energy of each wave system in a real lobe corresponding to the wave propagation direction and half in an identical artifact lobe propagating in the opposite direction.

Level 3 average wave spectra are truncated to 65 × 65-point arrays centered on zero wavenumber with 0.00245-rad/m resolution and contained within ±0.08 rad/m in k-space. Fig. 19 shows two WSRA directional wave spectra from the Calwater 2015 flight on February 9, 2015, which have been Doppler- and variance-corrected but have not had the artifact lobes deleted. The bottom spectrum is from the middle of area A in Fig. 11 and the top spectrum is from the middle of area B. The large gray and black dots are in identical, symmetrical positions in both spectra. The real spectral lobes are in the right half-plane and the dots were positioned to approximate the average locations of the real spectral peaks in the two spectra.

In the time it takes to acquire the wave topography data to produce a directional wave spectrum, waves propagating in the aircraft flight direction will move away from the aircraft and appear to have a longer wavelength while waves propagating in the opposite direction will appear shorter in the wave topography. Waves propagating in other directions will generally appear to have both different wavelengths and directions of propagation.

The real and artifact lobes in the encounter directional wave spectrum (L3) generated by the two-dimensional FFT applied to the WSRA wave topography are perfectly symmetrical. The Doppler correction applied to an encounter spectrum assumes all spectral components are real. A spectral lobe propagating in the aircraft flight direction would have too long a wavelength in the encounter spectrum and would be shifted to higher wavenumbers. A spectral lobe propagating in the opposite direction would have too short a wavelength in the encounter spectrum and would be shifted to lower wavenumbers.

In general, the first-order correction shifts all wave components in the aircraft flight direction. The real lobes are shifted into their proper positions and the artifact lobes are shifted in the wrong direction, out of their symmetrical positions. In Fig. 19 it is apparent that the artifact lobes are shifted in the aircraft flight direction.

Fig. 20 shows two WSRA directional wave spectra from Hurricane Irene which have been Doppler- and variance-corrected but have not had the artifact lobes deleted. The spectra are from passes through the eye flying south (top) and northwest (bottom). The two data sets were separated by about 73 min and Hurricane Irene had traveled 20 km in that time. But if the characteristics of the storm did not change, the storm-relative wave field could be assumed unchanged.

Since the wave spectra were unimodal in this case, the automated header information identifying two wave components was retained in Fig. 20. The northwest wave component was the real lobe and had the same propagation direction (−63°) in both spectra. The peak wavelengths agreed within 18 m and the wave heights differed by 0.4 m. The southeast wave component was the artifact lobe. In the two spectra, their propagation directions differed by 17°. The wave heights differed by 1.3 m and the wavelengths differed by 195 m. As in Fig. 19, the artifact lobes are shifted out of their symmetrical positions in the aircraft flight direction.

If the aircraft were changing the flight direction 90° to the right as it did in Fig. 19, it would be optimum to accomplish

that by turning 270° toward the left so the two flight tracks would cross. During recon missions, due to time constraints, aircrafts do not make 270° turns; but 90° turns will result in a significant separation of the locations where the aircraft is flying straight and level before and after a turn. In the case of Fig. 19, it was 19 km. The wave field for Fig. 19 was varying slowly spatially. In a hurricane flight, the wave field generally changes rapidly spatially and sometimes both the real and artifact lobes are mismatched when the aircraft changes flight direction. But even in that instance, correlating the directions in which the lobes are mismatched with the flight directions can generally sort things out.

The technique shown in Figs. 19 and 20 demonstrates that it is possible to identify the real and artifact spectral lobes without *a priori* information about ocean wave fields whenever the WSRA wave spectra are collected from significantly different flight tracks over the same area of the ocean. However, to delete the artifact lobes in complex ocean wave field conditions throughout a hurricane, the real-time WSRA processing uses a simplified hurricane wind model [22], [23] to generate a wind-forcing pattern to predict the propagation direction for waves of various lengths for every measurement point inside the hurricane. The inputs to the model are the maximum wind speed, the radius of maximum wind (RMW), and up-to-date track of the hurricane eye. A 12-h history is the minimum requirement for the track of the hurricane eye and, if the RMW is unknown, 40 km is used as a default. Even though a model's prediction of the wave propagation direction can at times be significantly different than the actual wave direction, the results are generally effective because the prediction only has to be a little closer to the real lobe than the artifact lobe.

In 10-km steps outward from the WSRA observation point, the square of the model wind component directed toward the observation point is integrated on every 5° azimuth to generate an effective wind forcing pattern. For each 10-km step outward from the observation point, an earlier position of the hurricane is used, determined by the transit time to the observation point at the group velocity of the ocean wavelength under consideration. The centroid of the wind forcing pattern specifies the direction that waves of that wavelength are predicted to be propagating.

Wind forcing patterns are computed for eight different wavelengths: 366, 256, 197, 160, 135, 116, 102, and 91 m. The distances from the observation point that the wind is integrated over vary from 516 km (12 h) for the longest wavelength to 129 km (6 h) for the shortest. The dots in Fig. 21 indicate the 65 × 65 locations in the WSRA directional wave spectra. The alternating black and gray dots identify the eight regions of the spectrum that the predicted wave propagation directions are applied to.

The elimination of the artifact lobes is done in an iterative fashion. The peak of the L3 directional wave spectrum is determined. The two peak locations (real and artifact) are Doppler-corrected, which changes both their wavelengths and propagation directions. The peak whose propagation direction is nearest to the propagation direction assigned to the closest of the eight wavelengths (Fig. 21) is deemed the real lobe.

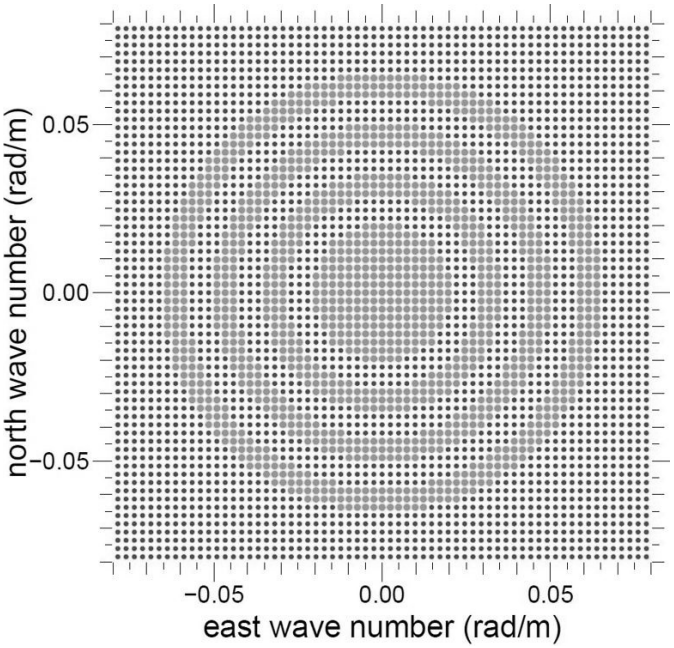

Fig. 21. WSRA directional wave spectrum points with alternating black and gray dots identifying the eight spectral regions that wind-forcing predicted wave propagation directions are applied to.

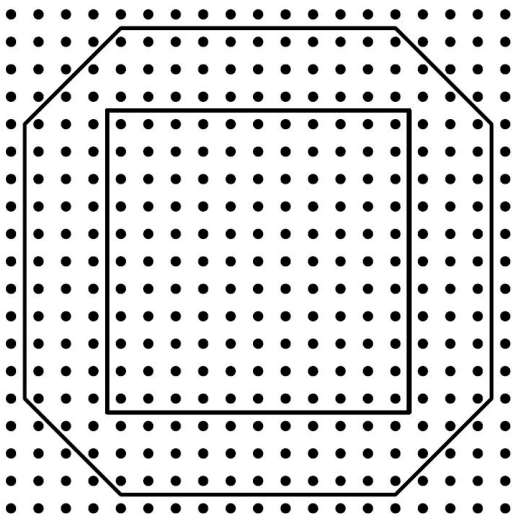

Fig. 22. Regions surrounding an L3 real spectral maximum that are transferred to the output spectrum automatically (square) and potentially (octagon) if the variance continues to decrease.

It and the surrounding nonzero values within the square in Fig. 22 are transferred to an output array. Nonzero values between the square and the octagon are also transferred to the output array if they continue to decrease.

All values transferred to the output array and the corresponding artifact values in the L3 spectrum are zeroed out and the peak of what remains is determined. The procedure is repeated until the peak of what remains is below 0.5% of the original L3 spectrum peak.

For a nonhurricane flight, the orientations of the eight predicted wave propagation directions are simply specified. It allows for the possibility that a long-wavelength swell could

be propagating eastward while a short wavelength wind-driven system propagated westward. For the February 9, 2015 flight off the California coast, the wave systems were propagating in the right half-plane and the propagation directions for the eight wavelengths were all set to 90°. In a more complex situation, the wave propagation direction specifications could vary temporally and/or spatially.

APPENDIX B
DESCRIPTION OF LEVEL-4 NETCDF FILE VARIABLES

WSRA Data Products (Variable Names Are in Boldface):

1) **Directional_wave_spectrum** contains all (Level 4) directional ocean wave spectra from the flight. The artifact spectral lobes have been deleted in the Level-4 spectra and the real spectral lobes have been Doppler-corrected for the motion of the waves during the data acquisition interval and variance-corrected for distortions in the wave topography measured by the WSRA. Variance values are in m^2.
2) **Directional_wave_spectrum_180** contains directional wave spectra with both real and artifact spectral lobes which have been Doppler-corrected and variance-corrected.
3) **Dominant_wave_direction** is the propagation direction of the dominant wave field in degrees.
4) **Dominant_wave_height** is the SWH of the ocean dominant wave field in meters.
5) **Dominant_wave_wavelength** is the peak wavelength of the ocean dominant wave field in meters.
6) **Peak_spectral_variance** is the peak spectral variance in m^2 of the Level 4 directional ocean wave spectra.
7) **Rainfall_rate** is the five independent values of rain rate (mm/h) determined at −20-, −10-, 0-, 10-, 20-s displacements relative to the observation time.
8) **Rainfall_rate_median** is the median value of the five values in rainfall_rate.
9) **Sea_surface_mean_square_slope** is the five independent values of mss determined at −20-, −10-, 0-, 10-, 20-s displacements relative to the observation time.
10) **Sea_surface_mean_square_slope_median** is the median value of the five values in sea_surface_mean_square_slope.
11) **Sea_surface_wave_significant_height** (SWH) in meters.
12) **Secondary_wave_direction** is the propagation direction of the secondary ocean wave field in degrees, if one exists.
13) **Secondary_wave_height** is the SWH of the secondary ocean wave field in meters, if one exists.
14) **Secondary_wavelength** is the peak wavelength of the secondary ocean wave field in meters, if one exists.
15) **WSRA_computed_roll** is the average WSRA computed aircraft roll attitude determined at −20-, −10-, 0-, 10-, 20-s displacements relative to the observation time.

WSRA Processing Parameters:

1) **Dominant_to_secondary_partition_angle** indicates the North relative angle as a boundary between the dominant and secondary wave fields if two have been identified.
2) **Wave_direction_predicted** is the predicted direction of propagation for eight wavelengths (366, 256, 197, 160, 135, 116, 102, 91 m) computed to aid in deleting artifact lobes.
3) **SWH_correction_ratio** is the ratio of the corrected SWH to the SWH estimated from WSRA Level-2 data.

Ancillary Data:

1) **Time** is the time of the observation in seconds since the start of the observations specified in the variable's attribute "units."
2) **Latitude** in degrees.
3) **Longitude** in degrees.
4) **Platform_course** is the North-relative aircraft track angle received from aircraft IWG1 in degrees.
5) **Platform_orientation** is North-relative aircraft heading received from aircraft IWG1 in degrees.
6) **Platform_radar_altitude** is the aircraft altitude in meters determined by the WSRA.
7) **Platform_speed_wrt_ground** is the aircraft ground speed received from aircraft IWG1 in m/s.
8) **Hurricane_eye_distance_east** is the distance east of the hurricane eye in km.
9) **Hurricane_eye_distance_north** is the distance north of the hurricane eye in km.
10) **Wind_direction** is the upwind direction at the aircraft altitude in degrees.
11) **Wind_speed** at the aircraft altitude in m/s.

Dimensions:

1) **Trajectory** = UNLIMITED; //data sequence index.
2) **Wavenumber_east** = 65; // 65 spectral wavenumber values along the east axis within ±0.08 rad/m.
3) **Wavenumber_north** = 65; // 65 spectral wavenumber values along the north axis within ±0.08 rad/m.
4) **Wavelength** = 8; // eight wavelengths (366, 256, 197, 160, 135, 116, 102, and 91 m).
5) **Obs** = 5; // time offset (−20, −10, 0, 10, 20 s) relative to the observation time.

ACKNOWLEDGMENT

The development of the WSRA prototype was initiated in 2006 with funding from the NOAA/SBIR program with a matching grant from the Center for Advanced Sensor and Communication Antennas (CASCA) at the University of Massachusetts Amherst to develop its microstrip phased-array antenna. Subsequent funding from NOAA's JHT program supported the development of the software for real-time reporting of WSRA data products. For the last eight years, WSRA operation during the hurricane seasons, two NOAA experiment campaigns (Clearwater and ATOMIC), and numerous system improvements were funded with annual contracts from the NOAA Earth System Research Laboratories (ESRL).

The NOAA Aircraft Operations Center installs and operates the WSRA.

REFERENCES

[1] J. E. Kenney, E. A. Uliana, and E. J. Walsh, "The surface contour radar, a unique remote sensing instrument," *IEEE Trans. Microw. Theory Techn.*, vol. MTT-27, no. 12, pp. 1080–1092, Dec. 1979.

[2] E. J. Walsh, D. Hancock, D. Hines, and J. Kenney, "Surface contour radar remote sensing of wave spectra," in *Proc. Conf. Directional Wave Spectra Appl. Symp.*, R. Wiegel, Ed., 1981, pp. 281–298.

[3] E. J. Walsh, D. W. Hancock, D. E. Hines, R. N. Swift, and J. F. Scott, "Directional wave spectra measured with the surface contour radar," *J. Phys. Oceanogr.*, vol. 15, no. 5, pp. 566–592, May 1985.

[4] E. J. Walsh, D. Hancock, D. Hines, R. Swift, and J. Scott, "An observation of the directional wave spectrum evolution from shoreline to fully developed," *J. Phys. Oceanogr.*, vol. 19, no. 5, pp. 670–690, 1989.

[5] C. L. Parsons, E. J. Walsh, and D. C. Vandemark, "Topographic mapping using a multibeam radar altimeter," *IEEE Trans. Geosci. Remote Sens.*, vol. 32, no. 6, pp. 1170–1178, Nov. 1994.

[6] C. W. Wright *et al.*, "Hurricane directional wave spectrum spatial variation in the open ocean," *J. Phys. Oceanogr.*, vol. 31, no. 8, pp. 2472–2488, Aug. 2001.

[7] E. J. Walsh *et al.*, "Hurricane directional wave spectrum spatial variation at landfall," *J. Phys. Oceanogr.*, vol. 32, no. 6, pp. 1667–1684, Jun. 2002.

[8] I.-J. Moon, I. Ginnis, T. Hara, H. L. Tolman, C. W. Wright, and E. J. Walsh, "Numerical simulation of sea surface directional wave spectra under hurricane wind forcing," *J. Phys. Oceanogr.*, vol. 33, no. 8, pp. 1680–1706, Aug. 2003.

[9] P. G. Black *et al.*, "Air–sea exchange in hurricanes: Synthesis of observations from the coupled boundary layer air–sea transfer experiment," *Bull. Amer. Meteorol. Soc.*, vol. 88, no. 3, pp. 357–374, Mar. 2007.

[10] S. S. Chen, J. F. Price, W. Zhao, M. A. Donelan, and E. J. Walsh, "The CBLAST-hurricane program and the next-generation fully coupled atmosphere-wave-ocean models for hurricane research and prediction," *Bull. Amer. Meteorol. Soc.*, vol. 88, pp. 311–317, Mar. 2007.

[11] Y. Fan, I. Ginis, T. Hara, C. W. Wright, and E. J. Walsh, "Numerical simulations and observations of surface wave fields under an extreme tropical cyclone," *J. Phys. Oceanogr.*, vol. 39, no. 9, pp. 2097–2116, Sep. 2009.

[12] P. A. Hwang and Y. Fan, "Effective fetch and duration of tropical cyclone wind fields estimated from simultaneous wind and wave measurements: Surface wave and air–sea exchange computation," *J. Phys. Oceanogr.*, vol. 47, no. 2, pp. 447–470, Feb. 2017, doi: 10.1175/JPO-D-16-0180.1.

[13] P. A. Hwang and E. J. Walsh, "Propagation directions of ocean surface waves inside tropical cyclones," *J. Phys. Oceanogr.*, vol. 48, no. 7, pp. 1495–1511, Jul. 2018, doi: 10.1175/JPO-D-18-0015.1.

[14] D. Barrick, "Rough surface scattering based on the specular point theory," *IEEE Trans. Antennas Propag.*, vol. 16, no. 4, pp. 449–454, Jul. 1968.

[15] D. Barrick, "Wind dependence of quasi-specular microwave sea scatter," *IEEE Trans. Antennas Propag.*, vol. 22, no. 1, pp. 135–136, Jan. 1974.

[16] G. R. Valenzuela, "Theories for the interaction of electromagnetic and oceanic waves ? A review," *Boundary-Layer Meteorol.*, vol. 13, nos. 1–4, pp. 61–85, Jan. 1978.

[17] B. Chapron, V. Kerbaol, D. Vandemark, and T. Elfouhaily, "Importance of peakedness in sea surface slope measurements and applications," *J. Geophys. Res., Oceans*, vol. 105, no. C7, pp. 17195–17202, Jul. 2000.

[18] A. G. Voronovich and V. U. Zavorotny, "Theoretical model for scattering of radar signals in Ku- and C-bands from a rough sea surface with breaking waves," *Waves Random Media*, vol. 11, no. 3, pp. 247–269, Jul. 2001.

[19] E. J. Walsh *et al.*, "The southern ocean waves experiment. Part III: Sea surface slope statistics and near-nadir remote sensing," *J. Phys. Oceanogr.*, vol. 38, no. 3, pp. 670–685, Mar. 2008.

[20] F. M. Ralph *et al.*, "CalWater field studies designed to quantify the roles of atmospheric rivers and aerosols in modulating U.S. west coast precipitation in a changing climate," *Bull. Amer. Meteorol. Soc.*, vol. 97, no. 7, pp. 1209–1228, Jul. 2016.

[21] C. W. Wright *et al.*, "Measuring storm surge with an airborne wide-swath radar altimeter," *J. Atmos. Ocean. Technol.*, vol. 26, no. 10, pp. 2200–2215, Oct. 2009.

[22] H. E. Willoughby, R. W. R. Darling, and M. E. Rahn, "Parametric representation of the primary hurricane vortex. Part II: A new family of sectionally continuous profiles," *Monthly Weather Rev.*, vol. 134, no. 4, pp. 1102–1120, 2006.

[23] J. A. Zhang and E. W. Uhlhorn, "Hurricane sea surface inflow angle and an observation-based parametric model," *Monthly Weather Rev.*, vol. 140, no. 11, pp. 3587–3605, Nov. 2012.

Ivan PopStefanija (Member, IEEE) received the B.S.E.E. degree in electrical engineering and telecommunications from the University of Ljubljana, Ljubljana, Yugoslavia, in 1982, and the Ph.D. degree in electrical and computer engineering from the University of Massachusetts, Amherst, MA, USA, in 1991.

From June 1983 to August 1984, he was a Research Associate with the Institute Mihailo Pupin, Belgrade, Yugoslavia. From July 1991 to August 1996, he was a Research Engineer and Senior Research Fellow at the University of Massachusetts Microwave Remote Sensing Laboratory (MIRSL). At MIRSL, he specialized in the area of high-speed data acquisition and the use of multifrequency microwave radars to remotely sense ocean surface currents. He was involved in the development of key instruments for use in the international SAXON-FPN and SAXON-CLT experiments. Since 1992, he has been with ProSensing Inc. (formerly Quadrant Engineering), Amherst, where he served as the President from 1993 to 1996. In 2000, with two other partners, he founded ProSensing Inc., a firm which specializes in custom-built radar and radiometer systems for a wide range of environmental remote sensing applications. At ProSensing Inc., he is a Managing Partner and a Principal Investigator on a number of projects. Over the years, he developed the data acquisition and real-time processing systems for several remote sensing instruments, including high-resolution polarimetric millimeter-wave cloud profiling radars and a modified military phased array radar to be used for severe weather surveillance. He led the development of remote sensing instruments, such as the airborne combined C-band scatterometer and Doppler wind profiler and the wide swath radar altimeter for measuring directional ocean wave spectra.

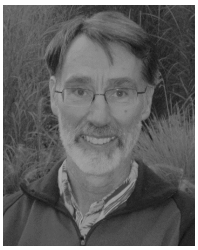

Christopher W. Fairall is a Physicist at the NOAA's Physical Sciences Laboratory, Boulder, CO, USA, where he heads the Boundary Layer Observations and Processes Team. He works in unraveling the mysteries of how the ocean and atmosphere battle as part of the Earth's climate system from El Nino to hurricanes. He has spent decades developing and deploying air–sea interaction observing systems for NOAA ships and aircraft and has participated in nearly 70 research field programs.

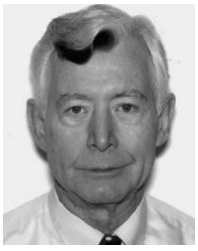

Edward J. Walsh (Life Senior Member, IEEE) received the B.S. and Ph.D. degrees in electrical engineering from Northeastern University, Boston, MA, USA, in 1963 and 1967, respectively.

From 1967 to 1970, he served at the National Aeronautics and Space Administration (NASA) Electronics Research Center, Cambridge, MA, USA, both as a civil servant and while on active duty in the U.S. Army as a Captain in the Signal Corps. From 1970 to 2009, he was with the NASA Wallops Flight Facility, Goddard Space Flight Center, Greenbelt, MD, USA, where he was involved in radar remote sensing of the sea. From 1982 to 2009, he was on assignment for NASA at the National Oceanic and Atmospheric Administration Physical Sciences Laboratory, Boulder, CO, USA, for cooperative research. Since retiring from NASA, he has maintained an affiliation with NOAA/PSL, using the NOAA Wide Swath Radar Altimeter to measure sea surface roughness, directional wave spectra, and rain rate in hurricanes and other environments.

Dr. Walsh received the NASA Medal for Exceptional Scientific Achievement in 1975 and the NRL Alan Berman Research Publication Award in 2001. He is a member of the IEEE Geoscience and Remote Sensing Society and Commission F of the U.S. National Committee of URSI.